

Experimental ~~calibration~~ assessment of a ~~MPLNET/Micro-Pulse Lidar~~ system in comparison with ~~EARLINET~~ lidar measurements for aerosol optical properties retrieval

5 Carmen Córdoba-Jabonero^{1*}, Albert Ansmann², Cristofer Jiménez², Holger Baars²,
María-Ángeles López-Cayuela¹, and Ronny Engelmann²

¹Instituto Nacional de Técnica Aeroespacial (INTA), Atmospheric Research and Instrumentation Branch,
Torrejón de Ardoz, 28850-Madrid, Spain

²Leibniz Institute for Tropospheric Research (TROPOS), Leipzig, Germany

10 *Correspondence to:* Carmen Córdoba-Jabonero (cordobajc@inta.es)

Abstract. Simultaneous observations of a polarized Micro-Pulse Lidar (P-MPL) system, currently operative within MPLNET (NASA Micro-Pulse Lidar Network), with two referenced EARLINET (European Aerosol Research Lidar Network) lidars, running at Leipzig site (Germany, 51.4°N 12.4°E, 125 m a.s.l.), were performed during a comprehensive two-month field campaign in summer 2019. A calibration assessment regarding the overlap (OVP) correction of the P-MPL signal profiles and its impact in the retrieval of the optical properties is achieved, describing also the experimental procedure used. The optimal lidar-specific OVP function for correcting the P-MPL measurements is experimentally determined, highlighting that the OVP function as delivered by the P-MPL manufacturer cannot be used. Among the OVP functions examined, the averaged one between those obtained from the comparison of the P-MPL observations with those of the other two referenced lidars seems to be the best proxy at both near- and far-field ranges. In addition, the impact of the OVP function in the accuracy of the retrieved profiles of the total particle backscatter coefficient (PBC) and the particle linear depolarization ratio (PLDR) is examined. First, the volume linear depolarization ratio (VLDR) profile is obtained and compared to the reference lidars, showing it needs to be corrected by a small offset value within a good accuracy. Once P-MPL measurements are optimally OVP-corrected, the PBC profiles (and hence the PLDR ones) can be derived using the Klett-Fernald approach. In addition, an alternative method based on separation of the total PBC into their aerosol components is presented in order to estimate the total particle extinction coefficient (PEC) profile, and hence the Aerosol Optical Depth, from elastic P-MPL measurements. A dust event as observed at Leipzig in June 2019 is used for illustration. In overall, an adequate OVP function is needed to be determined in a regular basis to calibrate the P-MPL system in order to derive suitable aerosol products.

1 Introduction

Active remote sensing ~~are~~ an excellent tool for vertical monitoring of the atmosphere. In particular, aerosol lidar systems have demonstrated to be a suitable instrumentation for aerosol and cloud profiling in both the troposphere and stratosphere (e.g., Amiridis et al., 2015; Baars et al., 2019). Tropospheric aerosols are usually confined up to 7-8 km height under aerosol intrusion conditions (e.g., Mattis et al.,

2008; Pappalardo et al., 2013); otherwise, they are mostly concentrated in the ABL (around less than 1.5 km height). Indeed, lidar systems are widely used due to their high vertical spatial and temporal resolution.

Ground-based lidar networks are widely operative within the GAW (Global Atmospheric Watch) Aerosol Lidar Observations Network (GALION); among them, there are those extended at continental scales, as EARLINET (European AeRosol LIdar NETwork, www.earlinet.org; Pappalardo et al., 2014), which belongs also to the Aerosol Cloud and Trace Gases Research Infrastructure (ACTRIS, www.actris.eu), AD-NET (Asian Dust and aerosol lidar observation network, www-lidar.nies.go.jp/AD-Net; Sugimoto et al., 2008), and LALINET (a.k.a. ALINE, Latin American Lidar NETwork, www.lalinet.org; Barbosa et al., 2014). In addition, there are other aerosol networks like MPLNET (Micro-Pulse Lidar NETwork, mplnet.gsfc.nasa.gov; Welton et al., 2001), and PollyNET (POrtabLe Lidar sYstem NETwork, polly.tropos.de; Baars et al., 2016), whose sites are distributed around the world.


The use of polarization lidar options is increasing, since lidar depolarization measurements allow an improved typing of aerosols (dust, marine aerosol, anthropogenic pollution, volcanic ash, biomass burning, pollen, ...) as well as the separation of the optical properties (backscatter, extinction) of particle components within complex aerosol mixtures with vertical resolution (i.e., Ansmann et al., 2011; Burton et al., 2014; Yu et al., 2015; Sicard et al., 2016; Bohlmann et al., 2019). Therefore, new and promising methods based on the particle depolarization ratio were developed and used to derive aerosol profiles in terms of particle mass concentration, separately for the coarse and fine modes (i.e., Mamouri and Ansmann, 2017), in addition to estimate both the cloud-condensation nuclei (CCN) and ice-nucleating particle (INP) concentrations (i.e., Mamouri and Ansmann, 2016).

The atmospheric lidar scanning provides an accurate characterization at all ranges; however, lidar systems present an incomplete response in the near-range observational field due to the partial intersection of the field-of-view between the transmitter and the receiver for both the biaxial and coaxial lidar configurations. Therefore, lidar signal profiles must be corrected by this near-field loss of signal, that is, the overlap (OVP) correction (Wandinger and Ansmann, 2002); hence, the main concern is focused on their OVP calibration. The full-OVP height is different depending on the lidar system (e.g., Wandinger et al., 2016).

For the last two decades, the Micro-Pulse Lidar (MPL) (Campbell et al., 2002; Welton et al., 2002) has been the operative system within MPLNET; since a few years a polarized MPL version (P-MPL) is the standard lidar system. Both MPL and P-MPL observations have been widely performed for continuous monitoring of aerosols and clouds. In particular, MPL/P-MPL measurements were used for Atmospheric Boundary Layer (ABL) height retrievals (Lewis et al., 2013; Adame et al., 2015), for detection and characterization of both cirrus clouds (Luis et al., 2016; Córdoba-Jabonero et al., 2017) and Polar Stratospheric Clouds (PSC) (Campbell et al., 2008; Córdoba-Jabonero et al., 2013), for depolarization-based separation of the optical properties of different aerosol mixtures (Córdoba-Jabonero et al., 2018), for mass concentration estimation in comparison with forecast model simulations (Córdoba-Jabonero et al., 2019), for precipitation intensity determination (Li et al., 2018), and for assessment of the radiative effect of aerosols and cirrus clouds (Campbell et al., 2016; Córdoba-Jabonero et al., 2020a, 2020b), among others. Those works have demonstrated a good MPL performance in aerosol/cloud research.

However, the P-MPL system needs to be well characterized in terms of the backscattered lidar signal detected by both depolarization channels of the instrument (Flynn et al., 2007) in order to retrieve plausible aerosol optical properties.


80 The P-MPL is an elastic coaxial single-wavelength (532 nm) system and, differing from older MPL versions (Campbell et al., 2002; Welton et al., 2002), incorporates depolarization capabilities (Flynn et al., 2007). It can operate in routine continuous (24/7) mode. ~~From an instrumental point of view, the principal disadvantage~~ is reaching the full-OVP height at relatively high altitudes (typically at 4-6 km height; Campbell et al., 2002), being particularly relevant for tropospheric aerosol research. ~~Then, a qualified calibration must be performed in these systems.~~ In this framework, an experimental campaign was planned at the EARLINET Leipzig site (Germany, 51.4°N 12.4°E, 125 m a.s.l.), and devoted to compare P-MPL observations simultaneously with reference well-calibrated lidar measurements, and hence to determine the required P-MPL calibrations.

The aim of this work is fourfold: 1) to achieve an OVP calibration of the P-MPL system, i.e., to estimate
90 the experimental OVP function for correcting the P-MPL measurements; 2) to evaluate the volume linear depolarization ratio (VLDR), which is a lidar-derived parameter independent of OVP calibration; 3) to determine the P-MPL calibration-induced effects on the retrieval of optical properties, both the height-resolved particle backscatter coefficient (PBC) and particle linear depolarization ratio (PLDR); and 4)  to present an alternative method based on the separation of the PBC into their aerosol components (for
95 instance, as applied to a dust event) in order to estimate the vertical profile of the particle extinction coefficient (PEC) (and also the columnar total extinction, i.e., the Aerosol Optical Depth, AOD) from elastic P-MPL measurements. **Section 2** introduces the methodology for that purpose, where the field campaign performed, the P-MPL and reference lidar systems used and the data analysis of the experimental approaches applied are particularly described: the experimental procedure for accurately
100 characterizing the OVP function of the P-MPL systems, the correction of the VLDR, and the determination of the optical properties. Results are presented in **Section 3**, regarding the experimental estimation of the OVP function (error processing is described in **Annex A**), the evaluation of the VLDR, and the retrieval of the particle optical properties. A dust case as observed during the field campaign is used for that purpose. Main conclusions are presented in **Section 4**.

105 2 Methodology

2.1 Field campaign

A field campaign was performed at the EARLINET station of Leipzig, Germany (51.35°N 12.43°E, 125 m a.s.l.), managed by the Leibniz Institute for Tropospheric Research (TROPOS), for 6 weeks in June-July 2019 in order to mainly calibrate a P-MPL system with a special emphasis on the OVP correction.

110 The lidar system used was the MPL44245 unit (Sigma Space Corp.) routinely operating at the  LNET/El Arenosillo station at Huelva, Spain (ARN/Huelva, 37.1°N 6.7°W, 40 m a.s.l.), which is managed by the Spanish Institute for Aerospace Technology (INTA). Both stations are also AERONET (Aerosol RObotic NETwork, aeronet.gsfc.nasa.gov) sites, accomplishing the requisite for co-location of both networks. For the campaign, the ARN/Huelva P-MPL was temporarily deployed at Leipzig to be

compared against two EARLINET lidars routinely operative in this station. ~~Those are the~~ Polly (POrtabLe Lidar sYstem; Althausen et al, 2009; Engelmann et al., 2016) and ~~the~~ MARTHA (Multiwavelength Tropospheric Raman lidar for Temperature, Humidity, and Aerosol profiling; Jiménez et al., 2018) systems, ~~which were~~ used as reference ~~since~~ these lidars are well characterized with respect to EARLINET quality assurance standards (e.g., Böckmann et al., 2004; Pappalardo et al., 2004; Freudenthaler et al., 2008; Pappalardo et al., 2014; Wandinger et al., 2016; Belegante et al., 2016; Bravo-Aranda et al., 2016; Freudenthaler et al., 2016).

2.2 Lidar systems

2.2.1 Polarized Micro-Pulse Lidar (P-MPL)

The P-MPL system (Sigma Space corp., v. MPL-4B) is the standard lidar currently operating within MPLNET. It is an elastic lidar in coaxial configuration with depolarization capabilities operating in full-time (24/7) mode. Among the principal optical features, the laser emission at 532 nm, with a pulse energy of 6-8 μ J and a repetition rate of 2500 Hz, is ~~registered back~~ by a unique avalanche photodiode detector (APD), and the receiver system presents a field-of-view (FOV) of 80 μ rad full angle and the telescope diameter is 18 cm wide (Sigma Space Corp., MPL system information handbook, 2018). P-MPL vertical profiles are routinely acquired with 1-min integrating time and 15-m vertical resolution (in particular, for the ARN/Huelva P-MPL system) up to 30 km height. Main instrumental features of the P-MPL system are shown in **Table 1**.

Table 1: Main instrumental features of the lidar systems.

Lidar system	P-MPL	Polly	MARTHA
Routine operation	24/7	24/7	Supervised
Lidar Networks	MPLNET	EARLINET	EARLINET
Transmitter properties			
Wavelength (nm)	532	532 (*)	532 (*)
Energy/pulse (mJ)	0.006-0.008	400	1000
Pulse frequency (Hz)	2500	20	30
Eye-safety	Yes (ANSI Class II)	No	No
Receiver properties			
Telescope diameter (cm)	18	30	80
Telescope focal length (m)	2.23	0.89	9
FOV (μ rad full angle)	80.4	1000	500
Depolarization	Yes	Yes	Yes
Raman detection	No	Yes	Yes

(*) Used in this study.

~~A schematic optical configuration~~ of the MPL-4B version is shown in Flynn et al. (2007; see their Fig. 1). The laser light is alternatively transmitted linearly and circularly polarized to the atmosphere by switching between two retardation modes of a liquid crystal retarder (LCR). The corresponding backscattered light to those two polarized states by passing through a beam splitter to the single APD is ~~registered~~ in

dependence of the polarizing or depolarizing atmospheric particles leading to the suppression or not, respectively, of the orthogonally-detected signal w.r.t. the transmitted one into the single APD. Those two polarized signals are semi-simultaneously detected by alternatively switching in the basis of 50%/50% the LRC polarization mode (LCR switching time of 133 μ s) within every integrating minute. That is, those two signals are alternatively detected by the same APD, being recorded in two polarized ‘channels’: the 532-nm cross-signal (P_{cross}) and the 532-nm co-signal (P_{co}). Therefore, since no potentially existing efficiency or alignment differences are between those two ‘channels’ (as used a single APD), no corrections for these effects are required, as it is typically needed for ordinary two-channel polarization lidars. The measured lidar signal in those two polarized-channels is used to derive the P-MPL total range-corrected signal (RCS), P^{MPL} , following the methodology as described in Flynn et al. (2007), that is, $P^L = P_{co} + 2 P_{cross}$. More details on P-MPL signal correction and data processing can be found in Córdoba-Jabonero et al. (2018). Among the required instrumental P-MPL calibrations (Campbell et al., 2002; Welton et al., 2002), the OVP correction is a concerning issue, since the typical full-OVP height is reached at rather high altitudes (usually at 4-5 km height), affecting thus the aerosol profiles at ranges in the overall boundary layer and part of the troposphere. Therefore, after purchase, the P-MPL system is delivered with an original OVP function as provided by the manufacture company (Sigma Space Corp.), which, however, must be re-evaluated with time. Indeed, one of the goals of this work is to show the experimental procedure to obtain a new OVP calibration for the P-MPL lidar as compared to the original one, as will be exposed in Sect. 2.3.1, together to examine their effects in the retrieval of the optical properties.

2.2.2 PORTABLE Lidar sYSTEM (Polly)

The EARLINET Polly (PORTABLE Lidar sYSTEM) lidars are sophisticated, automated Raman-polarization lidar systems for scientific purpose, but with the advantage of an easy-to-use and well-characterized instrument with same design, same automated operation, and same centralized data processing delivering near-real-time data products. Polly systems have been developed and constructed at TROPOS with international partners since 2002 (Engelmann et al., 2016). All Polly lidar systems are designed for automatic and unattended operation in 24/7 mode. Meanwhile 12 Polly lidar systems are distributed around the globe (e.g., Baars et al., 2016). The Polly lidar system used as a reference in this comparison analysis, is the first one of the Polly family (Engelmann et al., 2016), which was substantially upgraded in 2016 (v. Polly_1v2). It emits linearly polarized light at 532 nm with 5 receiver channels: the elastically backscattered light at 532 nm, the cross-polarized light at 532 nm, the co-polarized light at 532 nm, the rotational-Raman scattered light near 532 nm, and the vibrational-rotational Raman scattered light at 607 nm. Its full-OVP is reached at around 300-500 m height, and thus preferred for the P-MPL OVP calibration purpose. Profiles of the Polly range-corrected signal, P^{Polly} , are routinely derived by using sample settings with 7.5-m vertical resolution and 30-sec temporal integration. The main instrumental features of the Polly system are shown in Table 1.

2.2.3 Multiwavelength Atmospheric Raman lidar for Temperature, Humidity, and Aerosol profiling (MARTHA)



The second EARLINET lidar, which is used as a reference in this work, is the dual receiver field-of-view (RFOV) Multiwavelength polarization/Raman lidar for Temperature, Humidity, and Aerosol profiling (MARTHA) (Mattis et al., 2008; Schmidt et al., 2013, Jimenez et al., 2019). MARTHA has a powerful laser, transmitting in total 1 J per pulse at a repetition rate of 30 Hz, with an 80-cm telescope diameter, being thus well designed for tropospheric and stratospheric aerosol observations. This lidar system measures Raman signals at 532 nm (P^{MARTHA} , which is that used in this work) and 607 nm and the polarization-sensitive 532-nm backscatter signals at two RFOVs so that, besides aerosol profiles, cloud microphysical properties can be retrieved from measured cloud multiple scattering effects. MARTHA can provide the 532-nm particle depolarization ratio as measured with the smaller RFOV, and also the 355-, 532-, and 1064-nm particle backscatter coefficients and the 355- and 532-nm extinction coefficient profiles with their corresponding lidar ratio profiles. For this large telescope (and a selected receiver FOV of 0.5 mrad) the overlap between laser beam and receiver FOV is complete around 2000 m height. The overlap profile of this laboratory lidar is very stable. The main instrumental features of the MARTHA system are shown in **Table 1**.

Experimental estimation of the overlap (OVP) function for P-MPL systems



The overlap (OVP) function, F_{OVP} , is used to correct the P-MPL RCS profiles, $P^{MPL}(z)$, at near-field altitudes, that is,

$$P_{OVP}^{MPL}(z) = P^{MPL}(z) / F_{OVP}(z), \quad (1)$$

where $P_{OVP}^{MPL}(z)$ represents the overlap-corrected P-MPL RCS profiles.

In this work, the experimental procedure to obtain F_{OVP} is based on the comparison of the $P^{MPL}(z)$ to either the Polly RCS profiles, $P^{Polly}(z)$, or the MARTHA ones, $P^{MARTHA}(z)$, which are both used as reference  der mostly clean and clear conditions. The Polly and MARTHA lidars present the advantage  ontrast to P-MPL system that the OVP function can be experimentally determined using their Raman channels (Wandinger and Ansmann, 2002). The P-MPL overlap function is thus calculated in terms of the ratio between the P-MPL and Polly/MARTHA RCS profiles, i.e.,

$$F_{OVP}(z) = P^{MPL}(z) / P^{ref}(z), \quad (2)$$

where $P^{ref}(z)$ denotes the reference RCS profiles as obtained from either Polly, $P^{Polly}(z)$, or MARTHA, $P^{MARTHA}(z)$, measurements. Both sets of RCS profiles are  malized at a given height (higher than the OVP altitude range), z_{norm} , and then $F_{OVP}(z)$ can be derived using **Eq. 2**. In particular, the full-OVP is obtained at the normalization height $z_{norm} = 9.5$ km a.g.l., being $F_{OVP}(z) = 1$ at $z \geq z_{norm}$. Errors associated to the estimation of $F_{OVP}(z)$ using this experimental approach are described in **Annex A**. Lidar observations performed under relatively clean conditions at the Leipzig station were used for the P-MPL OVP calibration. 

2.4 Determination of the aerosol optical properties

2.4.1 Retrieval of the particle backscatter coefficient, and both the volume and particle linear depolarization ratios

215 Once the OVP-corrected RCS is obtained from Eq. 1, the particle backscatter coefficient (PBC), β_p (km^{-1}) can be derived applying the Klett-Fernald (KF) algorithm (Fernald, 1984; Klett, 1985) by constraining the lidar ratio (LR, extinction-to-backscatter ratio) with the AERONET Aerosol Optical Depth (AOD) (elastic KF solution); hence, an effective LR, S_a^{eff} , is also obtained after convergence. The particle linear depolarization ratio (PLDR), δ_p , can be determined as follows,

$$220 \quad \delta_p = \frac{R \frac{(1+\delta_{mol})-\delta_{mol}(1+\delta^V)}{(1+\delta_{mol})-(1+\delta^V)}}{\dots} \quad (3)$$

where R is the backscattering ratio ($=\frac{(\beta_m+\beta_p)}{\beta_m}$, being β_m the molecular backscattering coefficient), δ^V is volume linear depolarization ratio (VLDR), and δ_{mol} is the molecular depolarization ratio ($\delta_{mol} = 0.0037$ for P-MPL systems; Behrendt and Nakamura, 2002). The PLDR is a lidar parameter widely used for defining the aerosol type (Burton et al., 2012; Gross et al., 2013), and for discriminating the particle size mode in some aerosol mixtures (Mamouri and Ansmann, 2017; Córdoba-Jabonero et al., 2018), among others. The determination of PBC is mainly depending on the OVP correction, as will be discussed in Sect. 3.3, and hence, the PLDR is also affected by OVP as well. Therefore, a good knowledge of the OVP function for the specific P-MPL system is also needed to obtain high-quality PBC and PLDR profiles.

230 The volume linear depolarization ratio (VLDR), δ^V , can be determined in relation with the P-MPL depolarization ratio, δ^{MPL} (Mishchenko and Hovenier, 1995; Gimmetstad, 2008). Following Flynn et al. (2007), δ^V can be easily expressed as

$$\delta^V = \frac{\delta^{MPL}}{\delta^{MPL}+1} = \frac{P_{cross}}{P_{co}+P_{cross}}, \quad (4)$$

235 where δ^{MPL} is defined as the ratio between P_{cross} and P_{co} , which are the two polarized RCS as described in Sect. 2.2.1. Since the OVP correction is equally applied to both those signals, the VLDR is unaffected by the OVP calibration. Hence, the VLDR for the P-MPL system was examined in comparison with that derived from Polly lidar measurements. All those variables are height-resolved, but the altitude dependence is omitted for simplicity. A dust case occurring for the night on 29-30 June 2019 at the Leipzig station is selected for that purpose.

240 2.4.2 Estimation of the particle extinction coefficient from elastic P-MPL measurements

The particle extinction coefficient (PEC) is also a height-resolved variable. However, its estimation from elastic lidar observations is a relevant concern due to the indetermination in solving the lidar equation for elastic systems. Usually, a KF solution can be derived by assuming an effective LR, S_a^{eff} , which is a constant in height value (see Sect. 2.4.1).

245 An alternative simple method is introduced in order to estimate the PEC profiles, $\sigma_p(z)$, from elastic P-MPL measurements without assuming a constant LR. That approach is based in the combination of the POLIPHON algorithm (Mamouri and Ansmann, 2017) with elastic P-MPL measurements, as described in Córdoba-Jabonero et al. (2018), and was similarly used in Giannakaki et al. (2020), showing the potential of elastic and polarized lidars for vertical extinction retrieval. A dust case study observed at Leipzig in

June 2019 is used for illustration of that methodology. First, the KF-derived PBC profile, $\beta_p(z)$, together with the PLDR one, $\delta_p(z)$, are used to separate the total β_p into the backscatter coefficients corresponding to each of those components within the dusty mixtures, that is, the dust coarse (Dc), β_{Dc} , dust fine (Df), β_{Df} , and non-dust (ND), β_{ND} . Note that $\beta_p = \beta_{Dc} + \beta_{Df} + \beta_{ND}$ (z-dependence is omitted for simplicity). Particular pure depolarization ratios of $\frac{1}{2}$, 0.16 and 0.05 were assumed, respectively, for the Dc, Df, and ND components (Córdoba-Jabonero et al., 2018; Ansmann et al., 2019). Hence, the vertical PEC profile for each separated component can be obtained by definition as

$$\sigma_i(z) = S_a^i \times \beta_i(z), \quad (5)$$

where i refers to the Dc, Df, and ND components, being S_a^i their corresponding pure LR, which are assumed to be 55 sr for $\frac{1}{2}$ and Df, and 25 sr for ND components (Ansmann et al., 2019). The vertical total PEC, $\sigma_p(z)$, can be calculated as follows

$$\sigma_p(z) = \sigma_{Dc}(z) + \sigma_{Df}(z) + \sigma_{ND}(z), \quad (6)$$

being

$$\tau = \sum_{n=1}^{n=N} \sigma_p(z_n) \Delta z \quad (7)$$

the total aerosol extinction in the overall atmospheric column (i.e., the AOD), where Δz is the lidar vertical resolution, and n indicates the discrete n-bin height-level ($n = 1, \dots, N$), being z_N the reference height under aerosol-free conditions.

3 Results

3.1 Experimental overlap function F_{OVP}

P-MPL observations were carried out from 6 June to 26 July 2019 at the Leipzig station during the field campaign. Simultaneous P-MPL and Polly/MARTHA measurements as performed under relatively clean conditions were selected for the OVP calibration purpose. The first comparison analysis corresponded to 12 hourly-averaged P-MPL and Polly RCS profiles within the night-time period from 28 June 2019 at 18UT to 29 June 2019 at 05UT (day-time values on 28 June at 18UT: AOD=0.10, Ångström exponent AE=1.59). The second one was related to the MARTHA night-time RCS measurements as averaged for 4 hours from 23 July 2019 at 21UT to 24 July 2019 at 00UT (day-time values on 23 July at 18UT: AOD=0.09, AE=1.33); P-MPL RCS profiles were also averaged during that same period for comparison. **Figure 1** shows the uncorrected by overlap P-MPL RCS profiles in comparison with the reference Polly (left panel) and MARTHA (right panel) ones for both those particular periods. The part of the P-MPL RCS profiling to be OVP-corrected is clearly highlighted ranging from the surface up to around 1.5 m height. Next, the experimental estimation of F_{OVP} for the P-MPL system is analysed in terms of the OVP-corrected RCS as obtained by applying each of those experimentally-estimated F_{OVP}^{Polly} and F_{OVP}^{MARTHA} (see **Sect. 2.3.1**), including also a comparison with the original one, $F_{OVP}^{original}$ (as provided by the manufacturer).

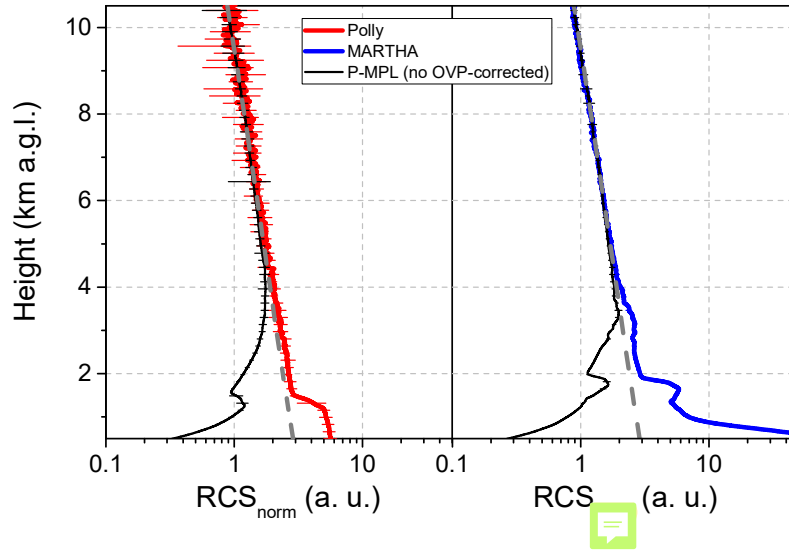


Figure 1: Comparison of the (left) reference Polly (red line; for clarity, the 12 P-MPL and Polly RCS profiles, from 28 June 18UT to 29 June 05UT, were averaged) and (right) MARTHA (blue line; 4 P-MPL and MARTHA RCS profiles, from 23 July 21UT to 24 July 00UT, were averaged) w.r.t. the uncorrected by overlap P-MPL profiles (black lines). Normalization height at 9.5 km a.g.l. The aerosol-free background signal is shown by a grey dashed line.

Figure 2 shows the experimental OVP functions, $F_{OVP}(z)$, as obtained from the comparison of the P-MPL RCS profiles w.r.t. Polly and MARTHA lidar measurements (top panel, F_{OVP}^{Polly} in red, and F_{OVP}^{MARTHA} in blue) (see Eq. 2) together with $F_{OVP}^{original}$; associated errors are also shown in the bottom panel. In addition, as both those OVP functions were obtained in two different days, temperature-related changes could be produced in the OVP calibration. Hence, the averaged $F_{OVP}^{av}(z)$ between both OVP functions is also calculated, and shown together the absolute and relative errors in Fig. 2, top and bottom panels, respectively). Details on the OVP error processing are described in Annex A. By comparing with the original OVP function, large discrepancies can be clearly observed, highlighting the change of $F_{OVP}(z)$ with time, mostly in the relevant 1-5 km height-range. Regarding the OVP functions F_{OVP}^{Polly} and F_{OVP}^{Marth} , differences are also found, mostly in the near-field range up to around 3 km height. However, by using $F_{OVP}^{av}(z)$ instead of one of two others for P-MPL RCS correction, its relative error is just $14 \pm 5\%$ in average from 0.3 up to 10 km height (see Fig. 2-bottom). Taking into account these errors, $F_{OVP}^{av}(z)$ can be the calibration function used for correcting the P-MPL RCS profiles at near-field heights, following the expression in Eq. 1, as it seems to be the best proxy for OVP correction of the P-MPL RCS profiles.

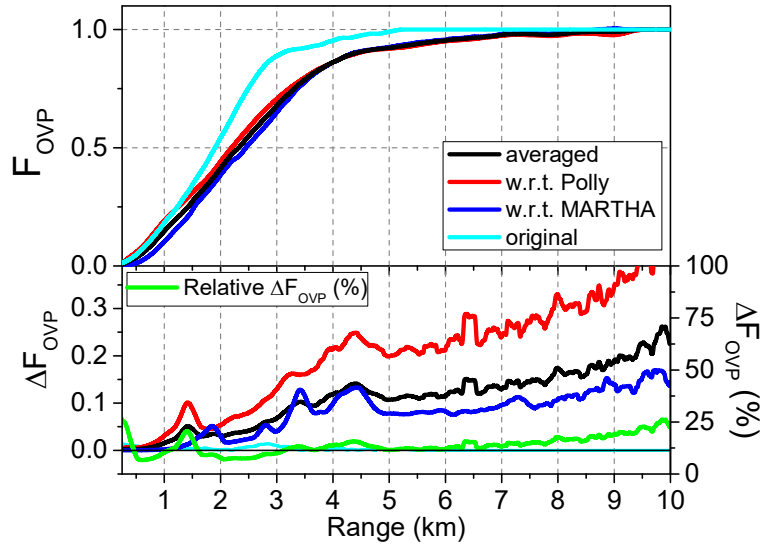


Figure 2: (Top) Experimental overlap functions, F_{OVP} , as obtained for two different days from the ratio between the P-MPL RCS profiles w.r.t. the Polly (F_{OVP}^{Polly} , red) and MARTHA (F_{OVP}^{MARTHA} , blue) ones, together with the averaged function (F_{OVP}^{av}) of both of them (black line); the original overlap function as provided by the manufacturer, $F_{OVP}^{original}$, is also included (cyan line). (Bottom) Errors, ΔF_{OVP} , associated to the OVP-function estimation for each comparison case: P-MPL w.r.t. Polly (red), P-MPL w.r.t. MARTHA (blue), and the averaged OVP function of both of them (black); the error for $F_{OVP}^{original}$ (cyan) and the relative error for F_{OVP}^{av} (green line) are also included.

The previous uncorrected and OVP-corrected P-MPL RCS profiles by using both F_{OVP}^{av} and $F_{OVP}^{original}$ are shown in **Figure 3**. Slightly differences are observed for the P-MPL RCS profiles as compared to those Polly and MARTHA ones by using F_{OVP}^{av} , despite it was calculated from averaging F_{OVP}^{Polly} and F_{OVP}^{MARTHA} , which were obtained from measurements on different days (only almost one month between them). Large differences are clearly found when $F_{OVP}^{original}$ is applied, mostly between 1.5 and 3 km height, evidencing that the OVP function as provided by the manufacturer is not applicable after some time for aerosol research, being necessary an regular OVP recalibration, as performed and described in this work. Once the P-MPL RCS profiles are OVP-corrected, the optical properties of the aerosols can be retrieved using inversion algorithms. OVP-induced effects in the inversion of the aerosol optical properties are analysed in **Sect. 3.3**.

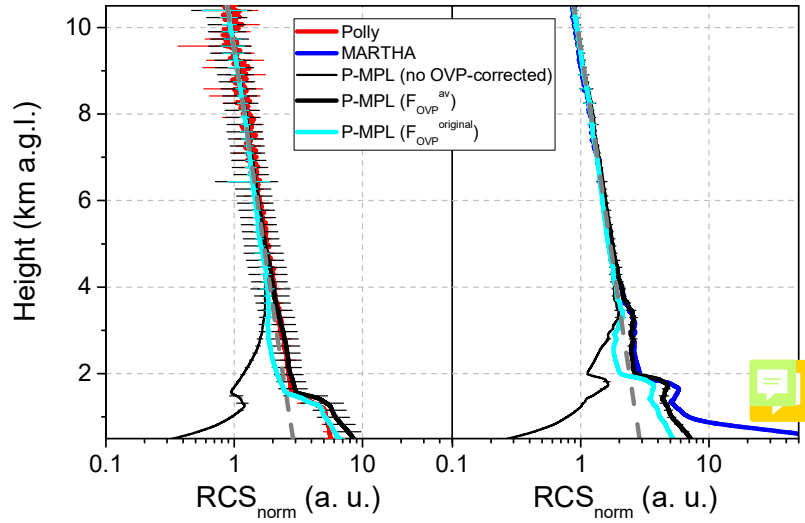


Figure 3: OVP-corrected (black thick lines) P-MPL RCS profiles by using F_{OVP}^{av} function and the uncorrected RCS ones (black thin lines), w.r.t. (Left) Polly (red line) and (Right) MARTHA (blue line) RCS profiles, together with the OVP-corrected ones by $F_{OVP}^{original}$ (cyan lines).

3.2 Volume linear depolarization ratio (VLDR)

Before analysing the OVP impact in the retrieval of the aerosol optical properties, the VLDR is also examined. Despite the VLDR is unaffected by the OVP calibration, it actually affects, together with the PBC, β_p , the PLDR, δ_p , estimation (see Sect. 2.3.2).

The P-MPL VLDR is calculated using Eq. 8 and compared with that derived from Polly measurements as reference, since TROPOS follows all quality assurance efforts regarding polarization lidar calibration tests in the Polly systems as recommended by EARLINET (Freudenthaler et al., 2008, 2016). A dust case observed at Leipzig site for the night on 29-30 June 2019 is examined for that purpose. Figure 4 shows the VLDR as obtained from both the δ_{MPL}^V and δ_{Polly}^V profiles as averaged from 18 to 23 UT on 29 June and from 00 to 05 UT on 30 June (for clarity, only averaged δ^V profiles are shown). The dust signature is clearly marked, showing a dust layer clearly confined between 3 and 6 km height, with a higher variability for the second interval due to the decay of dusty conditions at the end of that period, as reflected by a larger error uncertainty in time averaging. In overall, δ_{MPL}^V values are higher than those δ_{Polly}^V , peaking between 0.11 and 0.14 within the dust layer. Hence, the VLDR was averaged within several aerosol-free height-intervals, below and above that defined dust layer, to analyse potential changes and offsets. Those mean δ^V values (and their standard deviation, SD) are shown in Table 2.

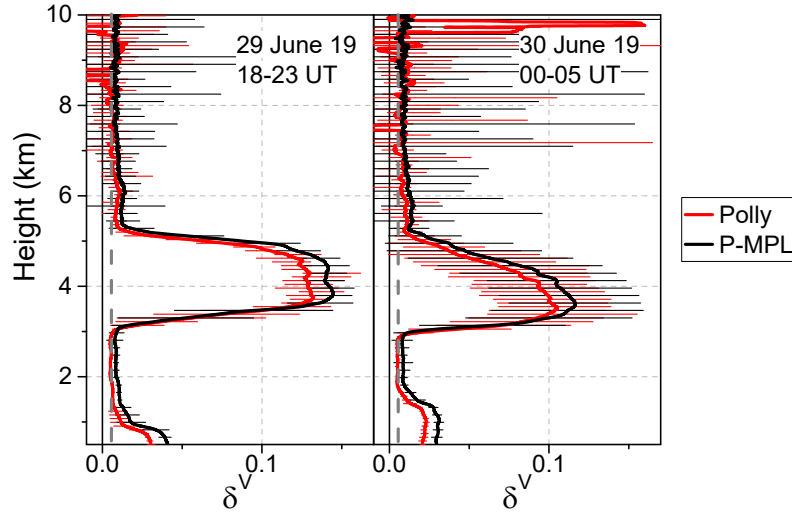


Figure 4: Volume linear depolarization ratio (VLDR), δ^V , as obtained from both the P-MPL (black line) and Polly (15-p smoothed red line) measurements carried out on: (left) 29 June 2019, as averaged from 18 to 23 UT, and (right) 30 June 2019, as averaged from 00 to 05 UT (error bars are also shown in black and red, respectively). The aerosol-free background δ^V is marked by a grey dashed line.

Table 2: Mean VLDR values together their standard deviation (SD) (and their relative SD error, in %) as obtained from the P-MPL and Polly measurements (δ_V^{MPL} and δ_V^{Polly} profiles) for aerosol-free height-intervals on 29-30 June 2019.

Height intervals (km)	δ^V , mean \pm SD (%SD)	
	P-MPL	Polly
1.5-2.5	0.0096 ± 0.0016 (16.6)	0.0057 ± 0.0002 (3.4)
7.0-8.0	0.0088 ± 0.0010 (10.8)	0.0057 ± 0.0037 (65.9)
8.0-9.0	0.0083 ± 0.0016 (19.7)	0.003 ± 0.016 (> 100)
Height-averaged	0.0089 ± 0.0005 (6.0)	0.0049 ± 0.0011 (23.1)

Looking at the results, δ_{Polly}^V presents larger errors than those for δ_{MPL}^V , as associated to a lower signal-to-noise ratio as height increases for the Polly measurements (no smoothing applied). This is reflected by the higher relative error (%SD) found for the Polly VLDR (23%) w.r.t. to that for the P-MPL (6%) when all the aerosol-free height-intervals are considered, being the mean δ^V values of 0.0089 ± 0.0005 (%SD: 6%) and 0.0049 ± 0.0011 (%SD: 23%), respectively, for the P-MPL and Polly VLDR. As a result, a constant offset, Δ ($= \delta_{Polly}^V - \delta_{MPL}^V$), can be assumed between δ_{MPL}^V and δ_{Polly}^V , obtaining $\Delta = -0.0040 \pm 0.0016$. This offset represents a correction to account for any slight mismatch in the transmitter and detector polarization planes and any impurity of the laser polarization state (Sassen, 2005), as also found in Córdoba-Jabonero et al. (2013) by characterizing the VLDR of a relatively older version (MPL-4) of the polarized MPL systems. Therefore, the P-MPL VLDR must be also corrected by that offset using the expression:

$$\delta_{MPL}^{V\ corr} = \delta_{MPL}^V + \Delta, \quad (8)$$

where δ_{MPL}^{Vcorr} is the corrected P-MPL VLDR profile.

Regarding the dust layer extended between 3.5 and 5.0 km height, as expected, a similar δ^V value to that obtained for the Polly VLDR ($\delta_{Polly}^V = 0.11 \pm 0.02$) is estimated for the corrected P-MPL VLDR, i.e., $\delta_{MPL}^{Vcorr} = 0.12 \pm 0.02$, as averaged within that dust layer. The corresponding PLDR to those δ^V are around 0.3 (as shown in **Sect. 3.3**), which are typical PLDR values for dust (Burton et al., 2012; Gross et al., 2013).

3.3 Particle backscatter coefficient (PBC) and particle linear depolarization ratio (PLDR)

The effect of the OVP correction on the P-MPL RCS is also analysed regarding the retrieval of the KF-derived β_p profiles, as obtained by applying both $F_{OVP}^{original}$ and F_{OVP}^{av} to the RCS. A dust event as observed at Leipzig on the night from 29 to 30 June 2019 (the same dust case as previously exposed in **Sect. 3.2**) is selected for that purpose. In addition, both PLDR, δ_p (see **Eq. 3**), and VLDR, δ^V (see **Eqs. 4 and 9**, Δ offset corrected) are estimated. The OVP-induced effect is illustrated, in particular, using the vertical hourly-averaged profiling observed on 29 June 2019 at 20-21 UT, corresponding to a well-separated two-layer dust case (dust optical depth of 0.061). **Figures 5 and 6** show the vertical profiles of β_p and δ_p (and δ^V), respectively, depending on the F_{OVP} applied, as retrieved from the P-MPL measurements together to those derived from Polly ones for the selected case.

Both P-MPL and Polly datasets show a dust layer clearly confined between around 3.5 and 5.0 km height. For comparison, in addition to the AOD-constrained KF solution for the PBC (reference height at 6.0 km, and reference backscatter coefficient of $10^{-7} \text{ Mm}^{-1} \text{ sr}^{-1}$) using $S_a^{eff} = 43 \text{ sr}$ (that obtained from Polly elastic measurements) (see **Figs. 5a and 5c**), β_p is also retrieved by using the Raman-derived LR ($S_a^{Raman} = 60 \text{ sr}$) for that dust layer as obtained from the night-time Polly Raman measurements (data not shown) (see **Figs. 5b and 5d**).

Table 3: Dust layer-averaged PBC, $\overline{\beta_p}$ ($\text{Mm}^{-1} \text{ sr}^{-1}$), and PLDR, $\overline{\delta_p}$, and the integrated backscatter, B (10^{-3} sr^{-1}), values, as obtained from P-MPL β_p and δ_p profiles on 29 June 2019 at 20-21 UT in dependence of the F_{OVP} applied for both the KF solutions (using S_a^{eff} and S_a^{Raman}). Corresponding Polly values are also included.

F_{OVP}	P-MPL						Polly		
	$S_a^{eff} = 43 \text{ sr}$			$S_a^{Raman} = 60 \text{ sr}$			$S_a^{eff} = 43 \text{ sr}$		
	$\overline{\beta_p}$	B	$\overline{\delta_p}$	$\overline{\beta_p}$	B	$\overline{\delta_p}$	$\overline{\beta_p}$	B	$\overline{\delta_p}$
F_{OVP}^{av}	0.93 ± 0.17	1.41 ± 0.16	0.32 ± 0.01	0.89 ± 0.15	1.35 ± 0.16	0.33 ± 0.01			
F_{OVP}^{Polly}	0.92 ± 0.16	1.40 ± 0.27	0.32 ± 0.01	0.88 ± 0.14	1.33 ± 0.27	0.33 ± 0.01	0.72 ± 0.16	1.08	0.29 ± 0.03
F_{OVP}^{MARTHA}	0.94 ± 0.17	1.43 ± 0.10	0.32 ± 0.01	0.90 ± 0.15	1.36 ± 0.10	0.32 ± 0.01			
$F_{OVP}^{original}$	0.87 ± 0.14	1.32 ± 0.05	0.33 ± 0.01	0.83 ± 0.12	1.26 ± 0.08	0.34 ± 0.02			

Regarding the dust layer, relatively small differences are found between Polly and P-MPL β_p profiles (see **Figs. 5a** and **5b**), at least within error uncertainties. In order to assess those differences between both datasets, the layer-averaged PBC, $\overline{\beta_p}$ ($\text{Mm}^{-1} \text{sr}^{-1}$), and the integrated backscatter, B (sr^{-1}), for this 3.5-5.0-km dust layer were calculated to be used as a proxy of the degree of agreement. Derived $\overline{\beta_p}$ and B values in dependence of F_{OVP} for both the KF solutions (using either S_a^{eff} or S_a^{Raman}) are shown in **Table 3**. In general, $\overline{\beta_p}$ and B are higher for P-MPL w.r.t. Polly retrievals. Concerning the KF solutions for P-MPL profiles, a better agreement is achieved when the S_a^{Raman} of 60 sr is applied (no AOD-constrain), i.e., lower differences for $\overline{\beta_p}$ and B are found w.r.t. Polly-retrieved values.

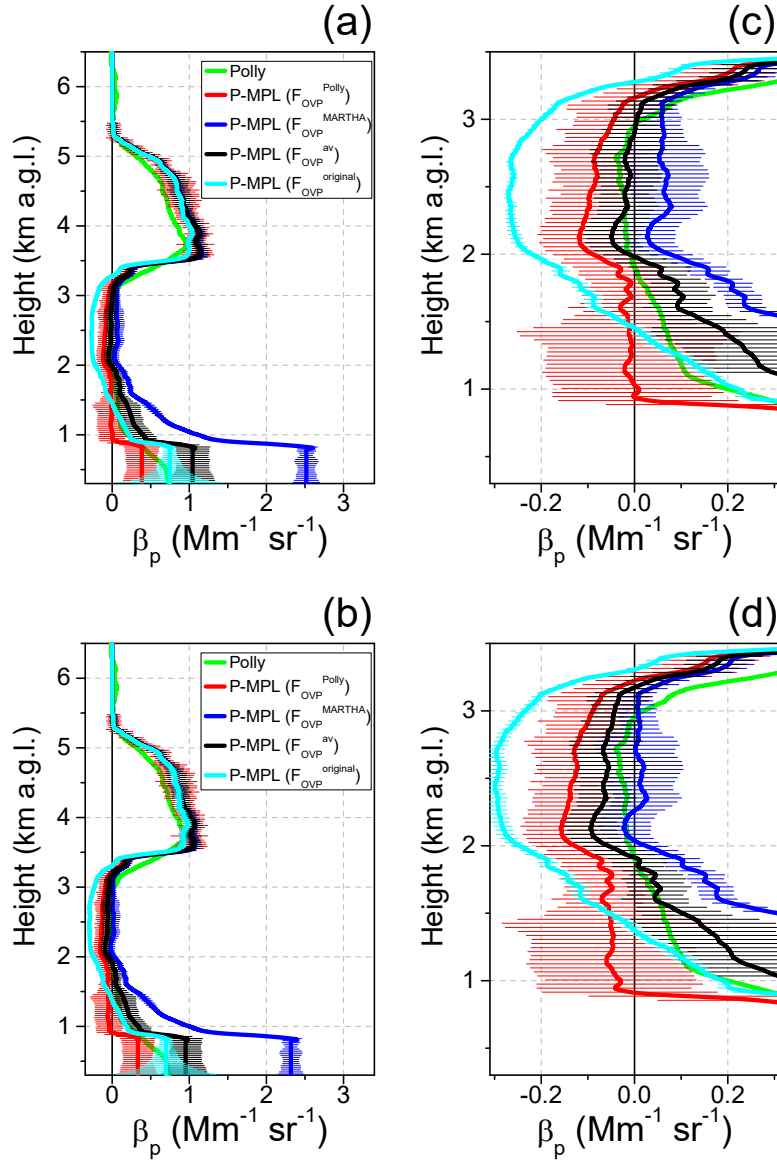


Figure 5: Dust case as observed on 29 June 2019 at 20:00-21:00 UT over Leipzig: Vertical particle backscatter coefficient (PBC), β_p , as retrieved in dependence of the OVP function applied to the P-MPL RCS: F_{OVP} w.r.t. to Polly (red) and MARTHA (blue) data and both the F_{OVP}^{av} (black) and $F_{OVP}^{original}$ (cyan) by using the KF solution with (a) the elastic AOD-constrained LR ($S_a^{eff} = 43$ sr), and (b) the Raman-retrieved LR ($S_a^{Raman} = 60$ sr) for the dust layer; and (c) and (d) the same as Fig. 5-a and 5-b, respectively, but highlighting the near-field

range of β_p between 0.5 and 3.5 km height (the x-axis is also accordingly scaled). Corresponding Polly-retrieved β_p profiles are also included (green lines).

Nevertheless, the KF retrieval is mostly affected at near-field ranges (up to 3 km height) (see **Figs. 5b** and **5d**), as expected, since the OVP correction is rather relevant at those ranges. Negative β_p values are predominantly found for the scenarios when the RCS is OVP-corrected by F_{OVP}^{Polly} and $F_{OVP}^{original}$, being more pronounced when the S_a^{Raman} is applied, since the LR to be applied in this height-interval must be closer to the elastic S_a^{eff} of 43 sr. The best fitting seems to be achieved by using F_{OVP}^{MARTHA} and F_{OVP}^{av} . Among those, however, results show that β_p profiles are in a better agreement by using F_{OVP}^{av} as compared to those Polly-derived β_p at ranges from around 1 km down (see **Figs. 5a** and **5c**). Relative $\beta_p[F_{OVP}^{av}]$ errors of 10-20% are obtained.

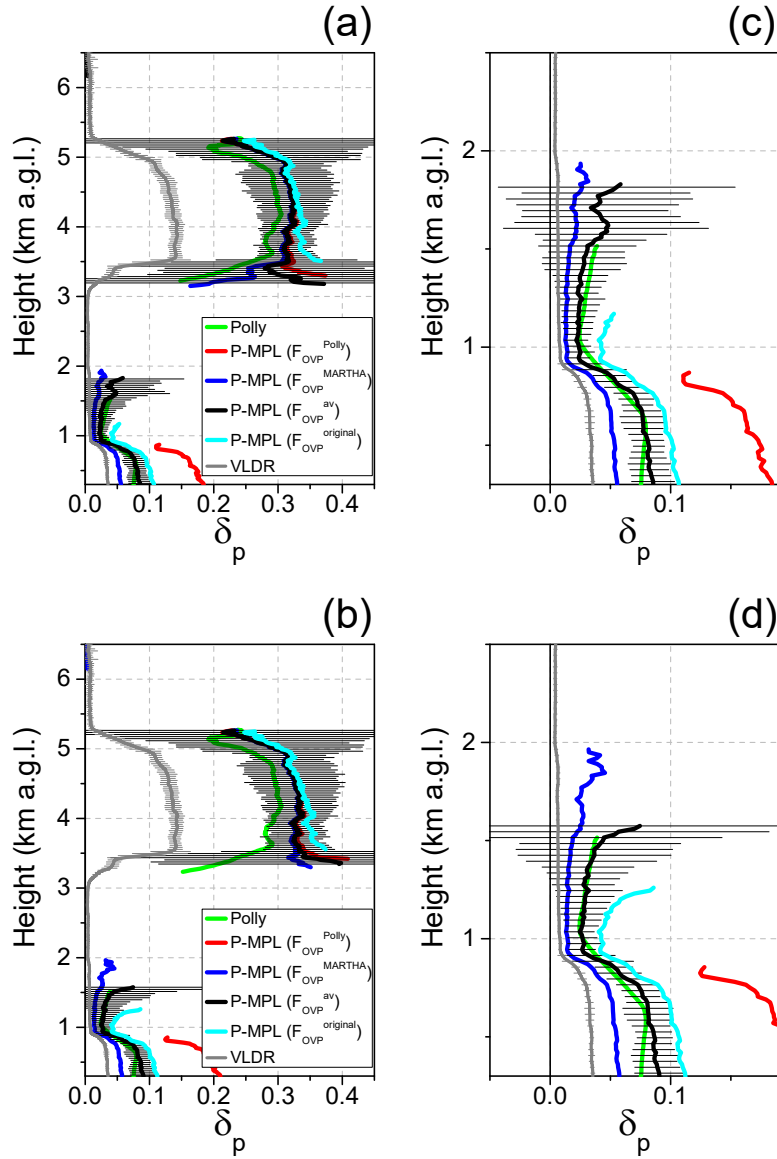


Figure 6: The same as Fig. 5, but for the vertical particle linear depolarization ratio (PLDR), δ_p , as retrieved from each $\beta_p[F_{OVP}]$ as shown in Fig. 5, and the VLDR, δ^V (grey line). The corresponding Polly-retrieved δ_p

profile is also included (green line). For clarity, only error bars are marked for $\delta_p[F_{OVP}^{av}]$ (black) and δ_p^{Polly} (green).

By examining the PLDR profiles, the dust signature is also clearly marked between around 3.5 and 5.0 km height, i.e., typical δ_p values for dust of around 0.3 are found (see Table 3), indicating a predominance of coarse particles. No large differences are found between Polly and P-MPL PLDR profiles for that layer (see Figs. 6a and 6b), with mean δ_p values of 0.29 (Polly) and 0.31-0.34 (P-MPL, depending on the F_{OVP} applied and the LR used) (see Table 3).

3.4 Particle extinction coefficient (PEC) retrieval for a dust case study

Once F_{OVP}^{av} is experimentally determined to correct the P-MPL RCS profiles (see Sect. 3.1), the total PBC can be retrieved by using the KF algorithm (a S_a^{eff} is also estimated against AERONET AOD constraint). The PLDR was also obtained by using the PBC and the corrected VLDR (see Sect. 3.2). In addition, using the approach as described in Sect. 2.4.2, the vertical total PEC profile, σ_p , and that corresponding to each component, σ_i ($i = Dc, Df, ND$), are obtained (see Eqs. 5-7), for instance, during a dusty event occurred at Leipzig in June 2019. For illustration, two different dust scenarios are examined: a well-separated pure dust layer observed on 29 June at 20-21 UT, and a mixed dust case occurred on 30 June at 16-17 UT.

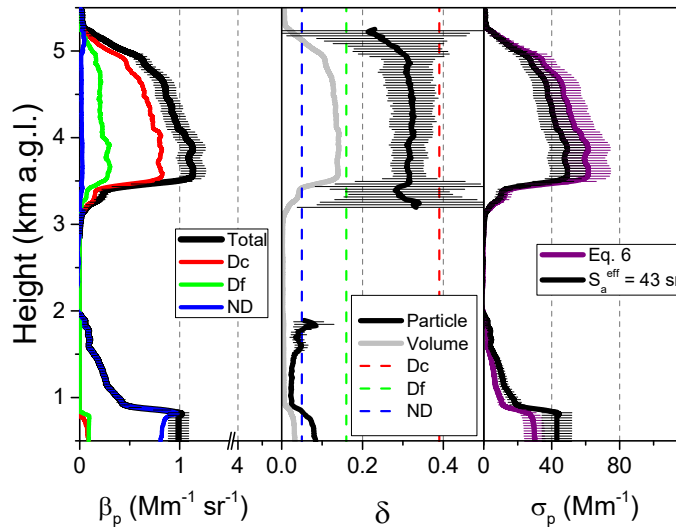


Figure 7: Dust scenario: well-differentiated pure dust layer on 29 June 2019 at 20-21 UT. Profiles of the (Left) particle backscatter coefficient: total (black), Dc (red), Df (green) and ND (blue); (Centre) linear depolarization ratio: particle (black) and volume (grey) together with those assumed for the pure components; and (Right) total particle extinction coefficient as obtained from: the use of an AERONET-constrained effective LR (black) and the sum of the particular PEC for each component (Dc, Df and ND) (Eq. 6, purple).

Figures 7 and 8 show the vertical profiles of both the total backscatter (and also that detached into the Dc, Df and ND components) and extinction coefficient together with the PLDR and VLDR, respectively, for each of those two selected cases. Differences in the vertical structure of the σ_p profiles between those

by using the KF-derived effective LR ($S_a^{eff} = 43$ and 25 sr are obtained, respectively, for the pure and mixed dust cases) and those by applying **Eq. (6)** are clearly shown for both dust scenarios.

In general, the KF solution for the total extinction seems to be underestimated, although τ values as obtained from **Eq. 7** differ from the effective total extinction (by using S_a^{eff}) in -6.4% and $+25.7\%$, respectively, for the pure ($\tau = 0.103$; **Fig. 7**) and mixed ($\tau = 0.264$; **Fig. 8**) dust cases. However, in those particular dust scenarios, the largest discrepancies are mostly found in layers with dust (Dc and Df) detection (see β_{Dc} and β_{Df} profiles, i.e., red and green lines, respectively, in **Figs. 7-left and 8-left**), regarding the difference in the LR applied between the effective value and that assumed typical for dust (55 sr). This is mainly observed for the dust mixed case (**Fig. 8**), as that LR difference is higher than that for the pure case. Indeed, the total extinction associated to layers with dust predominance is $+26.7\%$ and $+56.7\%$ of the corresponding effective value found, respectively, for the pure (3.5-5.0 km; see **Fig. 7-right**) and mixed (1.5-5.0 km; see **Fig. 8-right**) dust layers.

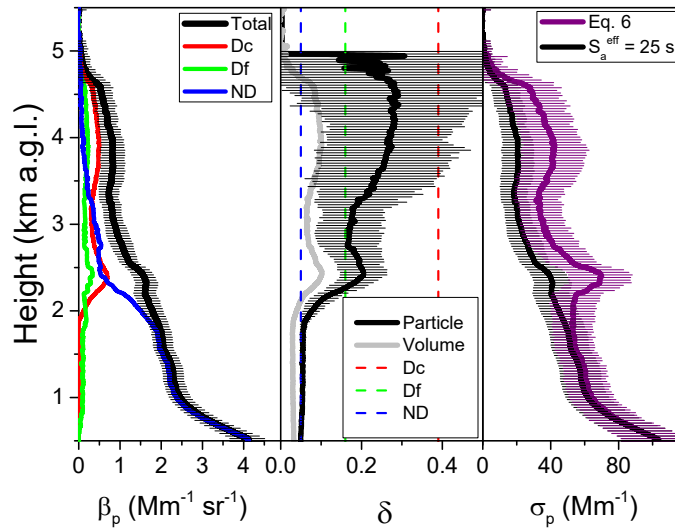


Figure 8: The same as Fig. 7, but for the dust scenario: mixed dust case on 30 June 2019 at 16-17 UT.

Therefore, the crucial point is concerning to the particular vertical aerosol extinction layering that is estimated by using either the effective KF-derived solution or the introduced depolarization-based method as observed in both dust scenarios. Indeed, this is especially relevant for the aerosol impact in atmospheric and climate research (atmospheric composition, radiative effect, cloud nucleation, ...). Moreover, this method can be easily used as an alternative approach for extinction retrieval in other elastic polarized lidar systems.

4 Conclusions

A comprehensive two-month field campaign has been performed in summer 2019 to characterize the performance of a polarized Micro-Pulse Lidar (P-MPL) system, and to check the quality of the retrieved products. Atmospheric observations with the P-MPL system, currently operative within MPLNET, have been examined against those from two referenced EARLINET lidars (Polly and MARTHA), which are

operative at Leipzig site (Germany, 51.4°N 12.4°E, 125 m a.s.l.) as managed by TROPOS. In particular, a characterization assessment in terms of the overlap (OVP) correction and its impact in the retrieval of the optical properties has been achieved. Furthermore, the volume linear depolarization ratio (VLDR) has also been cross-checked and corrections applied, allowing an accurate retrieval. The aim of this work has been focused on the determination of the lidar-specific true OVP function and on investigating in detail the accuracy of both the retrieved particle backscatter coefficient (PBC) and particle linear depolarization ratio (PLDR) profiles.

It has been highlighted that the OVP function as delivered by the P-MPL manufacturer cannot be used. The reasons are manifold, but an experimental assessment of the OVP calibration should be recommended for the MPL systems. The experimental procedure to determine the OVP function for the P-MPL system has been described in the basis of the comparison to reference lidars. The optimal OVP function for correcting our P-MPL measurements has been experimentally obtained, together with its uncertainties, under clean observational conditions from simultaneous P-MPL and Polly/MARTHA observations, and compared with the original one as provided by the manufacturer. In addition, depending on the OVP function applied, the calibration-induced effects on the retrieval of both the PBC and PLDR for the P-MPL system have been analysed for two KF solutions by using either the elastic (AOD-constrained) or the Raman-provided lidar ratios in comparison with those PBC and PLDR retrievals as obtained from simultaneous Polly observations.

Additionally, the VLDR has been also examined in comparison with the Polly VLDR regarding its effect in the PLDR determination. A suitable VLDR profile has been usually obtained, being only needed to be corrected by a small offset value, which has been also estimated.

Once P-MPL measurements were optimally OVP-corrected, the PBC, and also the PLDR, profiles have been accurately derived by using the KF solution (an effective LR is obtained in constraint with AERONET AOD). In addition, an alternative method has been introduced to derive the vertical particle extinction coefficient (PEC) profiles from elastic P-MPL measurements in combination with the POLIPHON algorithm by separating the optical properties into those corresponding to each component within aerosol mixtures. A dust event occurred at Leipzig in June 2019 is used for illustration, selecting two different dust scenarios: a well-differentiated dust layer and a mixed dust case. This is especially relevant for elastic lidars, as the P-MPL system among others, due to the indetermination in solving the lidar equation.

In overall, an adequate OVP function is needed to be determined in a regular basis in order to calibrate the P-MPL system and, hence, to derive suitable aerosol products (backscatter, depolarization, extinction).

Annex A

The experimental overlap (OVP) function, $F_{OVP}^{ref}(z)$, is obtained from the expression

$$F_{OVP}^{ref}(z) = P^{MPL}(z)/P^{ref}(z), \quad (A.1)$$

where $P^{MPL}(z)$ are the P-MPL RCS profiles, which are compared against those reference lidar measurements, $P^{ref}(z)$ (*ref* denotes either Polly or MARTHA) using the experimental approach as described in this work.

The error associated to the determination of the OVP function, ΔF_{OVP} , is obtained from error propagation calculations of the **Eq. A.1**. In this sense, it can be expressed as (z -dependence is omitted for simplicity, hereafter)

$$\Delta F_{OVP}^{ref} = F_{OVP}^{ref} \times \left[\frac{\Delta P^{MPL}}{P^{MPL}} + \frac{\Delta P^{ref}}{P^{ref}} \right], \quad (\text{A.2})$$

where ΔP^{MPL} and ΔP^{ref} are, respectively, the errors related to P^{MPL} and P^{ref} .

ΔP^{MPL} can be estimated as composed of two error contributions: one associated to instrumental corrections (energy fluctuations, instrumental calibrations, solar background, ...), ε^{MPL} , as described in Welton and Campbell (2002), and another one reflecting the atmospheric variability within the time-averaging performed of the P^{MPL} profiles, which is expressed by the standard deviation, sd^{MPL} ; hence, it can be obtained from the expression

$$\Delta P^{MPL} = \sqrt{(\varepsilon^{MPL})^2 + (sd^{MPL})^2}. \quad (\text{A.3})$$

Errors associated to the reference lidar measurements, ΔP^{ref} (*ref* is for either Polly or MARTHA), are represented by the standard deviation, as obtained from the corresponding time-averaging of P^{ref} profiles.

In this work, the averaged function between F_{OVP}^{Polly} and F_{OVP}^{MARTHA} is also calculated, i.e.,

$$F_{OVP}^{av} = \frac{F_{OVP}^{Polly} + F_{OVP}^{MARTHA}}{2}, \quad (\text{A.4})$$

being the error related to this function, ΔF_{OVP}^{av} , estimated as

$$\Delta F_{OVP}^{av} = \sqrt{\left(\frac{\Delta F_{OVP}^{Polly}}{2} \right)^2 + \left(\frac{\Delta F_{OVP}^{MARTHA}}{2} \right)^2}, \quad (\text{A.5})$$

where ΔF_{OVP}^{ref} (*ref* denotes either Polly or MARTHA) is the error as obtained from **Eq. A.2**.

Data availability. All data generated and analysed for this study are available from the authors upon reasonable request.

Author Contributions. CC-J and AA designed the study and wrote the original draft paper. CC-J, AA, CJ and HB provided data. CC-J and CJ performed data analysis with contributions from AA, HB, MAL-C and RE. All authors reviewed and edited the final version of the manuscript. All the authors agreed to the final version of the paper.

Competing interests. The authors declare that they have no conflict of interest.

Acknowledgements

This work was supported by the Spanish Ministry of Science, Innovation and Universities (MCIU) under grants PRX18/00137 (Programa "Salvador de Madariaga") and CGL2017-90884-REDT (ACTRIS-Spain), the Spanish Ministry of Science and Innovation (MICINN) (grant PID2019-104205GB-C21), and the H2020 program from the European Union (ACTRIS, GA n. 778349). MALC is supported by the INTA training fellowship programme. The MPLNET project is funded by the NASA Radiation Sciences Program and Earth Observing System.

References

- Adame, J. A., Córdoba-Jabonero, C., Sorribas, M., Toledo, D. and Gil-Ojeda, M.: Atmospheric boundary layer and ozone-aerosol interactions under Saharan intrusions observed during AMISOC summer campaign, *Atmos. Environ.*, 104, 205-216, <https://doi.org/10.1016/j.atmosenv.2014.12.036>, 2015.
- Althausen, D., Engelmann, R., Baars, H., Heese, B., Ansmann, A., Müller, D. and Komppula, M.: Portable Raman Lidar PollyXT for Automated Profiling of Aerosol Backscatter, Extinction, and Depolarization, *J. Atmos. Oceanic Technol.*, 26 (11), 2366-2378, <https://doi.org/10.1175/2009JTECHA1304.1>, 2009.
- Amiridis, V., E. Marinou, A. Tsekeri, U. Wandinger, A. Schwarz, E. Giannakaki, R. Mamouri, P. Kokkalis, I. Biniotoglou, S. Solomos, T. Herekakis, S. Kazadzis, E. Gerasopoulos, D. Balis, A. Papayannis, C. Kontoes, K. Kourtidis, N. Papagiannopoulos, L. Mona, G. Pappalardo, O. Le Rille, and A. Ansmann: LIVAS: a 3-D multi-wavelength aerosol/cloud climatology based on CALIPSO and EARLINET, *Atmos. Chem. Phys.*, 15, 7127-7153, <https://doi.org/10.5194/acp-15-7127-2015>, 2015.
- Ansmann, A., Tesche, M., Seifert, P., Groß, S., Freudenthaler, V., Apituley, A., Wilson, K. M., Serikov, I., Linné, H., Heinold, B., Hiebsch, A., Schnell, F., Schmidt, J., Mattis, I., Wandinger, U. and Wiegner, M.: Ash and fine-mode particle mass profiles from EARLINET-AERONET observations over central Europe after the eruptions of the Eyjafjallajökull volcano in 2010, *J. Geophys. Res.-Atmos.*, 116 (D20), <https://doi.org/10.1029/2010JD015567>, 2011.
- Baars, H., Kanitz, T., Engelmann, R., Althausen, D., Heese, B., Komppula, M., Preißler, J., Tesche, M., Ansmann, A., Wandinger, U., Lim, J.-H., Ahn, J. Y., Stachlewska, I. S., Amiridis, V., Marinou, E., Seifert, P., Hofer, J., Skupin, A., Schneider, F., Bohlmann, S., Foth, A., Bley, S., Pfüller, A., Giannakaki, E., Lihavainen, H., Viisanen, Y., Hooda, R. K., Pereira, S. N., Bortoli, D., Wagner, F., Mattis, I., Janicka, L., Markowicz, K. M., Achtert, P., Artaxo, P., Pauliquevis, T., Souza, R. A. F., Sharma, V. P., van Zyl, P. G., Beukes, J. P., Sun, J., Rohwer, E. G., Deng, R., Mamouri, R.-E. and Zamorano, F.: An overview of the first decade of PollyNET: an emerging network of automated Raman-polarization lidars for continuous aerosol profiling, *Atmos. Chem. Phys.*, 16 (8), 5111-5137, <https://doi.org/10.5194/acp-16-5111-2016>, 2016.
- Baars, H., Ansmann, A., Ohneiser, K., Haarig, M., Engelmann, R., Althausen, D., Hanssen, I., Gausa, M., Pietruczuk, A., Szkop, A., Stachlewska, I. S., Wang, D., Reichardt, J., Skupin, A., Mattis, I., Trickl, T., Vogelmann, H., Navas-Guzmán, F., Haeffele, A., Acheson, K., Ruth, A. A., Tatarov, B., Müller, D., Hu, Q., Podvin, T., Goloub, P., Veselovskii, I., Pietras, C., Haeffelin, M., Fréville, P., Sicard, M., Comerón,

580 A., Fernández García, A. J., Molero Menéndez, F., Córdoba-Jabonero, C., Guerrero-Rascado, J. L.,
 Alados-Arboledas, L., Bortoli, D., Costa, M. J., Dionisi, D., Liberti, G. L., Wang, X., Sannino, A.,
 Papagiannopoulos, N., Boselli, A., Mona, L., D'Amico, G., Romano, S., Perrone, M. R., Belegante, L.,
 Nicolae, D., Grigorov, I., Gialitaki, A., Amiridis, V., Soupiona, O., Papayannis, A., Mamouri, R.-E.,
 Nisantzi, A., Heese, B., Hofer, J., Schechner, Y. Y., Wandinger, U., and Pappalardo, G.: The
 585 unprecedented 2017–2018 stratospheric smoke event: decay phase and aerosol properties observed with
 the EARLINET, *Atmos. Chem. Phys.*, 19, 15183–15198, doi.org/10.5194/acp-19-15183-2019, 2019.

Barbosa, H. M. J., Lopes, F. J. S., Silva, A., Nisperuza, D., Barja, B., Ristori, P., Gouveia, D. A., Jimenez,
 C., Montilla, E., Mariano, G. L., Landulfo, E., Bastidas, A. and Quel, E. J.: The first ALINE
 measurements and intercomparison exercise on lidar inversion algorithms, *Opt. Pura Apl.*, 47 (2), 99–108,
 590 <https://doi.org/10.7149/OPA.47.2.99>, 2014.

Behrendt, A. and Nakamura, T.: Calculation of the calibration constant of polarization lidar and its
 dependency on atmospheric temperature, *Opt. Express*, 10 (16), 805–817,
<https://doi.org/10.1364/OE.10.000805>, 2002.

Belegante, L., Bravo-Aranda, J. A., Freudenthaler, V., Nicolae, D., Nemuc, A., Ene, D., Alados-
 595 Arboledas, L., Amodeo, A., Pappalardo, G., D'Amico, G., Amato, F., Engelmann, R., Baars, H.,
 Wandinger, U., Papayannis, A., Kokkalis, P. and Pereira, S. N.: Experimental techniques for the
 calibration of lidar depolarization channels in EARLINET, *Atmos. Meas. Tech.*, 11 (2), 1119–1141,
<https://doi.org/10.5194/amt-11-1119-2018>, 2018.

Böckmann, C., Wandinger, U., Ansmann, A., Bösenberg, J., Amiridis, V., Boselli, A., Delaval, A.,
 600 Tomasi, F. D., Frioud, M., Grigorov, I. V., Hågård, A., Horvat, M., Iarlori, M., Komguem, L., Kreipl, S.,
 Larchevêque, G., Matthias, V., Papayannis, A., Pappalardo, G., Rocadenbosch, F., Rodrigues, J. A.,
 Schneider, J., Shcherbakov, V. and Wiegner, M.: Aerosol lidar intercomparison in the framework of the
 EARLINET project. 2. Aerosol backscatter algorithms, *Appl. Opt.*, AO, 43 (4), 977–989,
<https://doi.org/10.1364/AO.43.000977>, 2004.

605 Bohlmann, S., Shang, X., Giannakaki, E., Filioglou, M., Saarto, A., Romakkaniemi, S. and Komppula,
 M.: Detection and characterization of birch pollen in the atmosphere using multi-wavelength Raman lidar
 in Finland, *Atmos. Chem. Phys.*, 19 (23), 14559, <https://doi.org/10.5194/acp-2019-635>, 2019.

Bravo-Aranda, J. A., Baumgardner, D., Guerrero-Rascado, J. L., Veselovskii, I., Lyamani, H.,
 Valenzuela, A., Olmo, F. J., Titos, G., Andrey, J., Chaikovsky, A., Dubovik, O., Gil-Ojeda, M. and
 610 Alados-Arboledas, L.: A comparative study of aerosol microphysical properties retrieved from ground-
 based remote sensing and aircraft in situ measurements during a Saharan dust event, *Atmos. Meas. Tech.*,
 9 (3), 1113–1113, 2016.

Burton, S. P., Ferrare, R. A., Hostetler, C. A., Hair, J. W., Rogers, R. R., Obland, M. D., Butler, C. F.,
 Cook, A. L., Harper, D. B. and Froyd, K. D.: Aerosol classification using airborne High Spectral
 615 Resolution Lidar measurements - methodology and examples, *Atmos. Meas. Tech.*, 5 (1), 73–98,
<https://doi.org/10.5194/amt-5-73-2012>, 2012.

Burton, S. P., Vaughan, M. A., Ferrare, R. A. and Hostetler, C. A.: Separating mixtures of aerosol types
 in airborne High Spectral Resolution Lidar data, *Atmos. Meas. Tech.*, 7 (2), 419–436,
<https://doi.org/10.5194/amt-7-419-2014>, 2014.

- 620 Campbell, J. R., Hlavka, D. L., Welton, E. J., Flynn, C. J., Turner, D. D., Spinhirne, J. D., Scott, V. S. and Hwang, I. H.: Full-Time, Eye-Safe Cloud and Aerosol Lidar Observation at Atmospheric Radiation Measurement Program Sites: Instruments and Data Processing, *J. Atmos. Oceanic Technol.*, 19 (4), 431-442, [https://doi.org/10.1175/1520-0426\(2002\)019<0431:FTESCA>2.0.CO;2](https://doi.org/10.1175/1520-0426(2002)019<0431:FTESCA>2.0.CO;2), 2002.
- Campbell, J. R. and Sassen, K.: Polar stratospheric clouds at the South Pole from 5 years of continuous
625 lidar data: Macrophysical, optical, and thermodynamic properties, *J. Geophys. Res.-Atmos.*, 113 (D20), <https://doi.org/10.1029/2007JD009680>, 2008.
- Campbell, J.R., S. Lolli, J.R. Lewis, Y. Gu, and E.J. Welton: Daytime Cirrus Cloud Top-of-Atmosphere Radiative Forcing Properties at a Midlatitude Site and their Global Consequence, *J. Appl. Meteorol. Clim.*, 5, 1667-1679, <https://doi.org/10.1175/JAMC-D-15-0217.1>, 2016.
- 630 Córdoba-Jabonero, C., Guerrero-Rascado, J. L., Toledo, D., Parrondo, M., Yela, M., Gil, M. and Ochoa, H. A.: Depolarization ratio of polar stratospheric clouds in coastal Antarctica: comparison analysis between ground-based Micro Pulse Lidar and space-borne CALIOP observations, *Atmos., Meas. Techniques*, 6 (3), 703-717, <https://doi.org/10.5194/amt-6-703-2013>, 2013.
- Córdoba-Jabonero, C., Lopes, F. J. S., Landulfo, E., Cuevas, E., Ochoa, H. and Gil-Ojeda, M.: Diversity
635 on subtropical and polar cirrus clouds properties as derived from both ground-based lidars and CALIPSO/CALIOP measurements, *Atmos. Res.*, 183, 151-165, <https://doi.org/10.1016/j.atmosres.2016.08.015>, 2017.
- Córdoba-Jabonero, C., Sicard, M., Ansmann, A., del Águila, A. and Baars, H.: Separation of the optical and mass features of particle components in different aerosol mixtures by using POLIPHON retrievals in
640 synergy with continuous polarized Micro-Pulse Lidar (P-MPL) measurements, *Atmos. Meas. Tech.*, 11 (8), 4775-4795, <https://doi.org/10.5194/amt-11-4775-2018>, 2018.
- Córdoba-Jabonero, C., Sicard, M., del Águila, A., Jiménez, M. and Zorzano, M.-P.: Performance of a dust model to predict the vertical mass concentration of an extreme Saharan dust event in the Iberian Peninsula: Comparison with continuous, elastic, polarization-sensitive lidars, *Atmos. Environ.*, 214, 116828, <https://doi.org/10.1016/j.atmosenv.2019.116828>, 2019.
- 645 Córdoba-Jabonero, C., Gómez-Martín, L., del Águila, A., Vilaplana, J. M., López-Cayuela, M.A., and Zorzano, M.-P.: Cirrus-induced shortwave radiative effects depending on their optical and physical properties: Case studies using simulations and measurements, *Atmos. Res.*, 246, 105095, 2020a.
- Córdoba-Jabonero, C., Sicard, M., López-Cayuela, M.-A., Ansmann, A., Comerón, A., Zorzano, M.-P.,
650 Rodríguez-Gómez, A., and Muñoz-Porcar, C.: Aerosol radiative effect during the summer 2019 heatwave produced partly by an inter-continental Saharan dust outbreak. 1. Shortwave dust-induced direct impact, *Atmos. Chem. Phys.*, acp-2020-1013 (in review), 2020b.
- Engelmann, R., Kanitz, T., Baars, H., Heese, B., Althausen, D., Skupin, A., Wandinger, U., Komppula, M., Stachlewska, I. S., Amiridis, V., Marinou, E., Mattis, I., Linné, H. and Ansmann, A.: The automated
655 multiwavelength Raman polarization and water-vapor lidar PollyXT: The neXT generation, *Atmos. Meas. Tech.*, 9, 1767-1784, <https://doi.org/10.5194/amt-9-1767-2016>, 2016.
- Fernald, F. G.: Analysis of atmospheric lidar observations: some comments, *Appl. Opt.*, 23 (5), 652, <https://doi.org/10.1364/AO.23.000652>, 1984.

- Flynn, C. J., Mendoza, A., Zheng, Y. and Mathur, S.: Novel polarization-sensitive micropulse lidar measurement technique, *Opt. Express*, 15 (6), 2785-2790, <https://doi.org/10.1364/OE.15.002785>, 2007.
- Freudenthaler, V.: The telecover test: A quality assurance tool for the optical part of a lidar system, Boulder, Colorado, 2008.
- Freudenthaler, V.: About the effects of polarising optics on lidar signals and the Delta 90 calibration, *Atmos. Meas. Tech.*, 9, 4181–4255, <https://doi.org/10.5194/amt-9-4181-2016>, 2016.
- Giannakaki, E., Kokkalis, P., Marinou, E., Bartsotas, N. S., Amiridis, V., Ansmann, A., and Komppula, M.: The potential of elastic and polarization lidars to retrieve extinction profiles, *Atmos. Meas. Tech.*, 13, 893-905, <https://doi.org/10.5194/amt-13-893-2020>, 2020.
- Gimmestad, G. G.: Reexamination of depolarization in lidar measurements, *Appl. Opt.*, 47 (21), 3795-3802, 2008.
- Groß, S., Esselborn, M., Weinzierl, B., Wirth, M., Fix, A. and Petzold, A.: Aerosol classification by airborne high spectral resolution lidar observations, *Atmos. Chem. Phys.*, 12 (10), 25983-26028, <https://doi.org/10.5194/acpd-12-25983-2012>, 2013.
- Jiménez, C., Ansmann, A., Donovan, D., Engelmann, R., Schmidt, J. and Wandinger, U.: Comparison between two lidar methods to retrieve microphysical properties of liquid-water clouds, *EPJ Web Conf.*, 176, 01032, <https://doi.org/10.1051/epjconf/201817601032>, 2018.
- Jiménez, C., Ansmann, A., Engelmann, R., Haarig, M., Schmidt, J. and Wandinger, U.: Polarization lidar: an extended three-signal calibration approach, *Atmos. Meas. Tech.*, 12 (2), 1077-1093, <https://doi.org/10.5194/amt-12-1077-2019>, 2019.
- Klett, J. D.: Lidar inversion with variable backscatter/extinction ratios, *Appl. Opt.*, AO, 24 (11), 1638-1643, <https://doi.org/10.1364/AO.24.001638>, 1985.
- Lewis, J. R., Welton, E. J., Molod, A. M. and Joseph, E.: Improved boundary layer depth retrievals from MPLNET, *J. Geophys. Res.-Atmos.*, 118 (17), 9870-9879, <https://doi.org/10.1002/jgrd.50570>, 2013.
- Lewis, J. R., Campbell, J. R., Welton, E. J., Stewart, S. A. and Haftings, P. C.: Overview of MPLNET Version 3 Cloud Detection, *J. Atmos. Oceanic Technol.*, 33 (10), 2113-2134, <https://doi.org/10.1175/JTECH-D-15-0190.1>, 2016.
- Lolli, S., L.P. D’Adderio, J.R. Campbell, M. Sicard, E.J. Welton, A. Binci, A. Rea, A. Tokay, A. Comeron, R. Barragan, J.M. Baldasano, S. Gonzalez, J. Bech, N. Afflitto, J.R. Lewis, and F. Madonna: Vertically Resolved Precipitation Intensity Retrieved through a Synergy between the Ground-Based NASA MPLNET Lidar Network Measurements, Surface Disdrometer Datasets and an Analytical Model Solution, *Remote Sens.*, 10, 1102; <https://doi.org/10.3390/rs10071102>, 2018.
- Mamouri, R.-E. and Ansmann, A.: Potential of polarization lidar to provide profiles of CCN- and INP-relevant aerosol parameters, *Atmos. Chem. Phys.*, 16 (9), 5905-5931, <https://doi.org/10.5194/acp-16-5905-2016>, 2016.
- Mamouri, R.-E. and Ansmann, A.: Potential of polarization/Raman lidar to separate fine dust, coarse dust, maritime, and anthropogenic aerosol profiles, *Atmos. Meas. Tech.*, 10 (9), 3403-3427, <https://doi.org/10.5194/amt-10-3403-2017>, 2017.
- Mattis, I., Müller, D., Ansmann, A., Wandinger, U., Preißler, J., Seifert, P. and Tesche, M.: Ten years of multiwavelength Raman lidar observations of free-tropospheric aerosol layers over central Europe:

Geometrical properties and annual cycle, *J. Geophys. Res.-Atmos.*, 113, D20202, <https://doi.org/10.1029/2007JD009636>, 2008.

Mishchenko, M. I., and J. W. Hovenier: Depolarization of light backscattered by randomly oriented nonspherical particles, *Opt. Lett.*, 20 (12), 1356-1358, 1995.

Pappalardo, G., Amodeo, A., Pandolfi, M., Wandinger, U., Ansmann, A., Bösenberg, J., Matthias, V., Amiridis, V., Tomasi, F. D., Frioud, M., Iarlori, M., Komguem, L., Papayannis, A., Rocadenbosch, F. and Wang, X.: Aerosol lidar intercomparison in the framework of the EARLINET project. 3. Raman lidar algorithm for aerosol extinction, backscatter, and lidar ratio, *Appl. Opt.*, AO, 43 (28), 5370-5385, <https://doi.org/10.1364/AO.43.005370>, 2004.

Pappalardo, G., Mona, L., D'Amico, G., Wandinger, U., Adam, M., Amodeo, A., Ansmann, A., Apituley, A., Arboledas, L. A., Balis, D., Boselli, A., Bravo-Aranda, J. A., Chaikovsky, A., Comeron, A., Cuesta, J., De Tomasi, F., Freudenthaler, V., Gausa, M., Giannakaki, E., Giehl, H., Giunta, A., Grigorov, I., Gross, S., Haeffelin, M., Hiebsch, A., Iarlori, M., Lange, D., Linne, H., Madonna, F., Mattis, I., Mamouri, R. E., McAuliffe, M. A. P., Mitev, V., Molero, F., Navas-Guzman, F., Nicolae, D., Papayannis, A., Perrone, M. R., Pietras, C., Pietruczuk, A., Pisani, G., Preissler, J., Pujadas, M., Rizi, V., Ruth, A. A., Schmidt, J., Schnell, F., Seifert, P., Serikov, I., Sicard, M., Simeonov, V., Spinelli, N., Stebel, K., Tesche, M., Trickl, T., Wang, X., Wagner, F., Wiegner, M., Wilson, K. M.: Four-dimensional distribution of the 2010 Eyjafjallajökull volcanic cloud over Europe observed by EARLINET, *Atmos. Chem. Phys.*, 13, 4429-4450, <https://doi.org/10.5194/acp-13-4429-2013>, 2013.

Pappalardo, G., Amodeo, A., Apituley, A., Comeron, A., Freudenthaler, V., Linné, H., Ansmann, A., Bösenberg, J., D'Amico, G., Mattis, I., Mona, L., Wandinger, U., Amiridis, V., Alados-Arboledas, L., Nicolae, D. and Wiegner, M.: EARLINET: towards an advanced sustainable European aerosol lidar network, *Atmos. Meas. Tech.*, 7 (8), 2389-2409, <https://doi.org/10.5194/amt-7-2389-2014>, 2014.

Sassen, K.: Lidar: range-resolved optical remote sensing of the atmosphere, chap. Polarization in lidar, no. 2 in *Springer Series in Optical Sciences*, Springer Science+ Business Media Inc., Springer-Verlag, New York., 2005.

Schmidt, J., Wandinger, U. and Malinka, A.: Dual-field-of-view Raman lidar measurements for the retrieval of cloud microphysical properties, *Appl. Opt.*, AO, 52 (11), 2235-2247, <https://doi.org/10.1364/AO.52.002235>, 2013.

Sicard, M., Izquierdo Miguel, R., Alarcón Jordán, M., Belmonte Soler, J., Comerón Tejero, A. and Baldasano Recio, J. M.: Near-surface and columnar measurements with a micro pulse lidar of atmospheric pollen in Barcelona, Spain, *Atmos. Chem. Phys.*, 16 (11), 6805-6821, <https://doi.org/10.5194/acp-16-6805-2016>, 2016.

Sigma Space Corporation, Micro-Pulse Lidar system information handbook, 2018.

Sugimoto, N., Matsui, I., Shimizu, A. and Nishizawa, T.: Lidar Network for Monitoring Asian Dust and Air Pollution Aerosols, in *IGARSS 2008 - 2008 IEEE International Geoscience and Remote Sensing Symposium*, vol. 2, p. II-573-II-576., 2008.

Wandinger, U. and Ansmann, A.: Experimental determination of the lidar overlap profile with Raman lidar, *Appl. Opt.*, AO, 41 (3), 511-514, <https://doi.org/10.1364/AO.41.000511>, 2002.

- Wandinger, U., Freudenthaler, V., Baars, H., Amodeo, A., Engelmann, R., Mattis, I., Groß, S., Pappalardo, G., Giunta, A., D'Amico, G., Chaikovsky, A., Osipenko, F., Slesar, A., Nicolae, D.,
740 Belegante, L., Talianu, C., Serikov, I., Linné, H., Jansen, F., Apituley, A., Wilson, K. M., de Graaf, M.,
Trickl, T., Giehl, H., Adam, M., Comerón, A., Muñoz-Porcar, C., Rocadenbosch, F., Sicard, M., Tomás,
S., Lange, D., Kumar, D., Pujadas, M., Molero, F., Fernández, A. J., Alados-Arboledas, L., Bravo-
Aranda, J. A., Navas-Guzmán, F., Guerrero-Rascado, J. L., Granados-Muñoz, M. J., Preißler, J., Wagner,
F., Gausa, M., Grigorov, I., Stoyanov, D., Iarlori, M., Rizi, V., Spinelli, N., Boselli, A., Wang, X., Lo
745 Feudo, T., Perrone, M. R., De Tomasi, F. and Burlizzi, P.: EARLINET instrument intercomparison
campaigns: overview on strategy and results, *Atmos. Meas. Tech.*, 9 (3), 1001-1023,
<https://doi.org/10.5194/amt-9-1001-2016>, 2016.
- Welton, E. J., Campbell, J. R., Spinhirne, J. D. and Scott III, V. S.: Global monitoring of clouds and
aerosols using a network of micropulse lidar systems, in *Lidar Remote Sensing for Industry and*
750 *Environment Monitoring*, vol. 4153, pp. 151–158, International Society for Optics and Photonics., 2001.
- Welton, E. J. and Campbell, J. R.: Micropulse Lidar Signals: Uncertainty Analysis, *J. Atmos. Oceanic*
Technol., 19 (12), 2089-2094, [https://doi.org/10.1175/1520-0426\(2002\)019<2089:MLSUA>2.0.CO;2](https://doi.org/10.1175/1520-0426(2002)019<2089:MLSUA>2.0.CO;2),
2002.
- Yu, H., Chin, M., Bian, H., Yuan, T., Prospero, J. M., Omar, A. H., Remer, L. A., Winker, D. M., Yang,
755 Y., Zhang, Y. and Zhang, Z.: Quantification of trans-Atlantic dust transport from seven-year (2007–2013)
record of CALIPSO lidar measurements, *Remote Sens. Environ.*, 159, 232-249,
<https://doi.org/10.1016/j.rse.2014.12.010>, 2015.